Electrical transport properties of Ti-doped Fe_2O_3(0001) epitaxial films

B. Zhao,[1,2] T. C. Kaspar,[1,*] T. C. Droubay,[1] J. McCloy,[3] M. E. Bowden,[4] V. Shutthanandan,[4] S. M. Heald,[5] and S. A. Chambers[1]
[1]*Fundamental and Computational Sciences Directorate, Pacific Northwest National Laboratory, Richland, Washington 99352, USA*
[2]*Department of Chemistry, University of Washington, Seattle, Washington 98195-1700, USA*
[3]*Energy and Environment Directorate, Pacific Northwest National Laboratory, Richland, Washington 99352, USA*
[4]*Environmental Molecular Sciences Laboratory, Pacific Northwest National Laboratory, Richland, Washington 99352, USA*
[5]*Advanced Photon Source, Argonne National Laboratory, Argonne, Illinois 60439, USA*
(Received 27 October 2011; published 30 December 2011)

The electrical transport properties for compositionally and structurally well-defined epitaxial α-$(Ti_xFe_{1-x})_2O_3$(0001) films have been investigated for $x \leqslant 0.09$. All films were grown by oxygen plasma-assisted molecular beam epitaxy using two different growth rates: 0.05–0.06 Å/s and 0.22–0.24 Å/s. Despite no detectable difference in cation valence and structural properties, films grown at the lower rate were highly resistive whereas those grown at the higher rate were semiconducting ($\rho = \sim 1\ \Omega \cdot \text{cm}$ at 25 °C). Hall effect measurements reveal carrier concentrations between 10^{19} and 10^{20} cm^{-3} at room temperature and mobilities in the range of 0.1 to 0.6 $\text{cm}^2/\text{V} \cdot \text{s}$ for films grown at the higher rate. The conduction mechanism transitions from small-polaron hopping at higher temperatures to variable-range hopping at a transition temperature between 180 and 140 K. The absence of conductivity in the slow-grown films is attributed to donor electron compensation by cation vacancies, which may form to a greater extent at the lower rate because of higher oxygen fugacity at the growth front.

DOI: 10.1103/PhysRevB.84.245325 PACS number(s): 73.61.Le, 81.15.Hi, 68.55.Ln

I. INTRODUCTION

Among the transition-metal oxides, hematite (α-Fe_2O_3) has been of significant interest due to its ubiquitous presence as an active surface for heterogeneous reactions in the terrestrial environment,[1] as well as possible utility in light-induced water splitting,[2,3] paleomagnetic dating,[4,5] and spin electronics.[6] Pure synthetic hematite is insulating with an experimental band-gap of ~2.2 eV.[7] With generally low conductivity limiting the usefulness of pure hematite, understanding and improving its transport properties has been of considerable interest.[8] Early experimental studies suggested that hematite exhibits unusually low electron mobility.[8,9] This result cannot be explained by a conventional band-like conduction picture in which itinerant electrons are delocalized and interact weakly with the lattice. Rather, a small polaron model, in which charge carriers polarize their immediate surroundings and hop between local energy minima, was invoked.[10] A hopping barrier of ~0.1 eV within the *ab*-plane has emerged from several theoretical and experimental studies.[11–13] Crystallographic anisotropies in the conductivity have also been observed and attributed to spin-flip scattering, which lowers the conductivity for transport along the *c* axis.[13,14] Although progress has been made on the theoretical front, experimental studies of transport in hematite have been limited due to difficulties resulting from the generally high resistivity of hematite and ambiguities associated with measurements on polycrystalline samples.[10,13,15]

Natural hematite can be weakly conductive due to the presence of impurities which act as unintentional electrical dopants.[16] Thus, an effective way of improving the conductivity of hematite through intentional doping is highly desirable. Transport investigations on well-characterized epitaxial films hold many advantages over those for natural bulk hematite. Building upon early work on the growth of pure hematite by molecular beam epitaxy (MBE) using a Cr_2O_3 buffer layer to grade the lattice mismatch and improve the crystallinity of the films,[17] Ti-doped hematite epitaxial films have been successfully deposited by oxygen-plasma-assisted molecular beam epitaxy (OPA-MBE).[6] Bench top four-point-probe conductivity measurements with spring-loaded contacts carried out at room temperature revealed a decrease in resistivity with increasing Ti concentration. The resistivity was found to be ~25 $\Omega \cdot$cm at a Ti concentration of 15 cation%.[6] Other methods for synthesizing Ti-doped hematite have also been utilized, including solid-state reaction,[18] sputtering,[19] and sol-gel.[20] However, transport measurements were limited in these investigations.

In this paper our goal has been to carry out a more comprehensive investigation of the transport properties for well-characterized Ti-doped hematite films. To this end, we have grown and characterized Ti-doped Fe_2O_3 epitaxial films with different Ti concentrations using two different growth rates. Interestingly, despite the absence of detectable differences in structure and cation valence at the two growth rates, the electrical properties are markedly different; the films grown at the higher rate are semiconducting, whereas those grown at the lower rate are highly resistive. By using a conductivity apparatus designed specifically for high-resistivity samples,[21] we have measured the temperature-dependent resistivity and Hall effect for the set of films grown at the higher rate. By making these measurements on compositionally and structurally well-defined materials, we can make meaningful comparisons with the expectations of various transport models.

II. EXPERIMENTAL DETAILS

Epitaxial Ti-doped hematite films $(Ti_xFe_{1-x})_2O_3$ ($x \leqslant 0.13$) were deposited through a 1-cm-diameter round shadow mask on α-Al_2O_3(0001) substrates using OPA-MBE. The substrates were cleaned by exposure to atomic oxygen from an electron cyclotron resonance oxygen plasma source in the OPA-MBE

 ©2011 American Physical Society

chamber at a pressure of 2×10^{-5} Torr for 30 min. The substrates were annealed at $\sim 500\,^{\circ}$C, as measured using a two-color infrared pyrometer, in the oxygen plasma for an additional 30 min to improve the surface crystallinity. A thin ($\sim$12 nm) Cr_2O_3 buffer layer was used to grade the lattice mismatch. Previous measurements revealed that this layer is nearly completely relaxed.[17] Both Cr_2O_3 and Ti-doped Fe_2O_3 layers were grown at a substrate temperature of $\sim 500\,^{\circ}$C and a chamber pressure of 2×10^{-5} Torr with the oxygen plasma activated. Cr was deposited using an electron-beam evaporator. The Cr flux was monitored and controlled using *in-situ* atomic absorption spectroscopy. Fe and Ti were evaporated using high-temperature effusion cells. The Fe flux was held constant for all films within each of the two sets (slow and fast grown), and the Ti flux was varied to achieve the desired doping level. Both Fe and Ti fluxes were checked using a quartz crystal oscillator prior to film growth. The actual $(Ti_xFe_{1-x})_2O_3$ growth rate for the slow-grown film set ranged from 0.055 Å/s to 0.059 Å/s, depending on doping level, and from 0.22 Å/s to 0.24 Å/s for the fast-grown films. Film thicknesses ranged from 50 nm to 70 nm.

Surface quality was monitored during growth using reflection high energy electron diffraction (RHEED). Charge states for Ti and Fe cations were determined by *in-situ* x-ray photoemission spectroscopy (XPS) using monochromatic Al Kα x rays. A low-energy electron flood gun was needed for the slow-grown films due to charging on these insulating samples. Dopant concentrations were determined by proton-induced x-ray emission (PIXE) with an incident beam of 2 MeV He^+. Microstructure and lattice parameters were determined using high-resolution x-ray diffraction (HRXRD) with a Philips X'Pert diffractometer equipped with a monochromatic Cu Kα x rays ($\lambda = 1.54056$ Å). Film thickness was measured using x-ray reflectivity (XRR). Charge states and local structure were determined by Fe and Ti K-edge x-ray absorption near-edge spectroscopy (XANES) and extended x-ray absorption fine structure (EXAFS) on the PNC-CAT beamline at the Advanced Photon Source.

Van der Pauw (VDP) resistivity and Hall measurements were made using a Quantum Design Physical Property Measurement System (PPMS) specially modified for high resistivity samples.[21] Ag pads were sputtered on the corners of each sample using a shadow mask, and Au-coated spring contacts were pressed into the Ag pads. Overlap of the silver pads with the film at each contact was small ($\sim$0.1 mm^2) to minimize errors in the VDP measurements. I-V curves at room temperature revealed that all contacts on the films were Ohmic. The temperature dependence of the resistivity was measured in the VDP configuration from 300 K to 50 K. Hall effect data were obtained with the magnetic field applied perpendicular to the film from -6 T to 6 T in the temperature range of 290 K to 190 K. DC current was applied in both directions at each field and temperature to eliminate intrinsic errors resulting from imperfect contact alignment.[22] Experimental errors commonly found in high resistivity samples due to film capacitance and temperature transients were minimized by waiting for the current and voltage signal to reach equilibrium after changing temperature, field, or current.

III. RESULTS AND DISCUSSION

A. Composition

Figure 1 shows a PIXE spectrum for a Ti cation concentration of $x = 0.08$, which was determined from the areal ratio of Ti and Fe Kα peaks fitted by the GUPIXWIN package.[23] Composition determination by Rutherford backscattering spectrometry (RBS) is difficult because He ions backscattered by Cr in the Cr_2O_3 film are inelastically scattered in the overlying $(Ti_xFe_{1-x})_2O_3$ film, resulting in decreases in their kinetic energies and an overlap of the Cr and Ti peaks. To avoid this complication, all compositional information used in this paper is based on PIXE rather than RBS.

B. Crystallographic properties

The RHEED patterns are very similar for all films regardless of deposition rate, revealing an epitaxial orientation to the substrate. The inset of Fig. 1 shows typical final RHEED patterns for slow- and fast-grown films with Ti concentrations of $x = 0.08$ and 0.09, respectively. Intensity modulations along the streaks reveal some surface roughness, as seen in previous studies of doped and undoped hematite grown by MBE.[6,17] This result is not unexpected considering the 1.55% in-plane lattice mismatch between bulk α-Fe_2O_3 and Cr_2O_3.

HRXRD patterns were collected from lattice planes parallel and oblique to the sample surface for both fast-grown and slow-grown Ti-doped films. These scans confirmed the single crystalline nature of the films and the epitaxial relationship with the underlying Al_2O_3 substrate, which was found to be $(0001)_{sub} \,||\, (0001)_{film}$ and $[\bar{2}110]_{sub} \,||\, [\bar{2}110]_{film}$. Grazing incidence XRD scans (not shown) of selected $(Ti_xFe_{1-x})_2O_3$ films revealed no secondary phases or polycrystalline reflections within the sensitivity limit of the measurement. Rocking curves of the (006) reflection for fast-grown $(Ti_{0.09}Fe_{0.92})_2O_3$ and slow-grown $(Ti_{0.08}Fe_{0.92})_2O_3$ films are shown in Fig. 2(a). The full width at half maximum (FWHM) for each film is narrow,

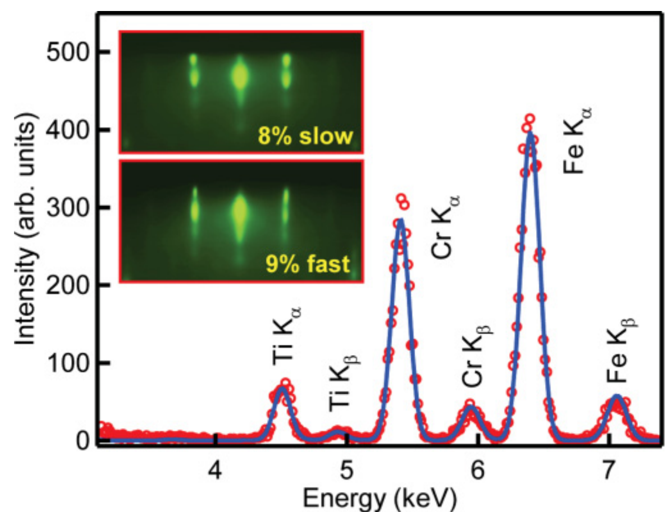

FIG. 1. (Color online) PIXE spectrum for a slow-grown $(Ti_xFe_{1-x})_2O_3/Cr_2O_3/Al_2O_3$, along with a fit generated using the GUPIXWIN software package revealing $x = 0.08$. Inset: final RHEED patterns for the slow-grown $(Ti_{0.08}Fe_{0.92})_2O_3$ film and a fast-grown $(Ti_{0.09}Fe_{0.91})_2O_3$ film.

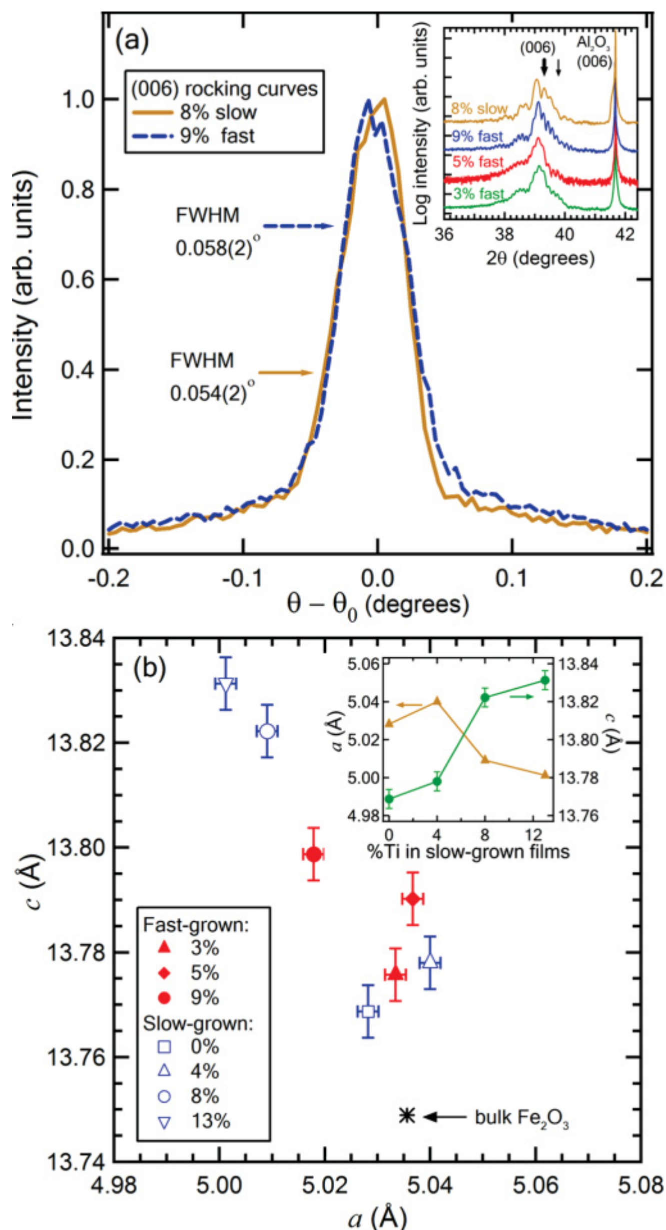

FIG. 2. (Color online) (a) HRXRD (006) rocking curves for the fast-grown $(Ti_{0.09}Fe_{0.91})_2O_3$ film and the slow-grown $(Ti_{0.08}Fe_{0.92})_2O_3$ film. Inset: HRXRD θ-2θ scans of fast-grown $(Ti_xFe_{1-x})_2O_3$ films ($x = 0.03, 0.05, 0.09$) and a slow-grown $(Ti_{0.08}Fe_{0.92})_2O_3$ film. Arrows indicate (006) peak positions for bulk Fe_2O_3 (wide) and bulk Cr_2O_3 (narrow). (b) Lattice parameters a and c for an undoped Fe_2O_3 film and the $(Ti_xFe_{1-x})_2O_3$ films. Error is estimated to be $\pm0.04\%$. Also shown are a and c for bulk Fe_2O_3 hematite. Inset: Lattice parameters plotted against Ti concentration for slow-grown $(Ti_xFe_{1-x})_2O_3$) films.

indicating excellent crystallinity with minimal mosaic spread. Notably, the rocking curve width is not strongly affected by the growth rate. The inset to Fig. 2(a) shows HRXRD θ-2θ scans for fast-grown $(Ti_xFe_{1-x})_2O_3$ films ($x = 0.03, 0.05, 0.09$) and a slow-grown $(Ti_{0.08}Fe_{0.92})_2O_3$ film. Laue oscillations reveal a high degree of crystalline quality in all cases.[24] Two frequencies are present in these oscillations. The higher frequency oscillations are associated with the relatively thicker $(Ti_xFe_{1-x})_2O_3$ layers, which are superimposed on the lower frequency oscillations coming from the thinner Cr_2O_3 layers. The broad, low-intensity shoulder at a lower 2θ value than the sharper peak from the $(Ti_xFe_{1-x})_2O_3$ layer is associated with the Cr_2O_3 buffer layer. An ilmenite-like phase[6] can be ruled out since $Fe_2O_3/Cr_2O_3/Al_2O_3$ deposited under the same conditions produced HRXRD patterns similar to those in the inset to Fig. 2(a). However, it is difficult to determine the Bragg peak position for the (006) reflection of the Cr_2O_3 buffer layer due to interference from the $(Ti_xFe_{1-x})_2O_3$ film and overlapping finite thickness oscillations. An out-of-plane expansion of Cr_2O_3 would indicate residual compressive in-plane strain associated with consecutive bilayer growth of $(Ti_xFe_{1-x})_2O_3$. Interestingly, deposition of a thin Cr_2O_3 buffer layer without a hematite overlayer resulted in a completely relaxed Cr_2O_3 film (not shown) as expected;[17] thermal expansion mismatch between the layers may play a role during sample cool-down in the $(Ti_xFe_{1-x})_2O_3/Cr_2O_3/Al_2O_3$ system.

Figure 2(b) plots the lattice parameters for all the $(Ti_xFe_{1-x})_2O_3$ films, determined by refining Voigt profiles simultaneously to the (1 0 10), (1 1 9), and (2 1 10) diffraction peaks. Also included are the lattice parameters for bulk hematite ($a = 5.04$ Å, $c = 13.75$ Å).[25] The lattice parameters of the $(Ti_xFe_{1-x})_2O_3$ films were not strongly affected by growth rate. The films exhibit an expansion in the out-of-plane direction, which correlates with increasing Ti concentration. This trend is most clearly seen for the slow-grown films, as plotted in the inset to Fig. 2(b). Ti substitution for Fe in the hematite lattice might be expected to cause lattice parameter contraction in both in-plane and out-of-plane directions, since the ionic radii for Ti^{4+} and high-spin Fe^{3+} are 0.61Å and 0.65Å, respectively.[26] However, ilmenite $FeTiO_3$, which consists of alternating layers of Ti^{4+} and Fe^{2+} in the (0001) direction, has a larger lattice ($a = 5.09$ Å and $c = 14.08$ Å)[27] than hematite. Another mechanism that can result in an out-of-plane expansion is incomplete relaxation of the epitaxial Ti-doped hematite film on the Cr_2O_3 buffer layer ($a = 4.92$ Å),[17] which would result in a small in-plane contraction and, therefore, an out-of-plane expansion. It is difficult to distinguish whether the observed trend with increasing Ti concentration is due to lattice expansion as the Ti-doped Fe_2O_3 film becomes more ilmenite-like or to a change in the elastic properties of the Ti-doped Fe_2O_3 films with increasing Ti concentration, which inhibits full epitaxial strain relaxation. From the lattice parameters plotted in Fig. 2(b), it appears that a combination of these factors may be at play.

C. Cation charge states and local structural environment

We show in Fig. 3(a) high-resolution Fe 2p and Ti 2p core-level XPS spectra for three fast-grown films and a representative slow-grown $(Ti_{0.08}Fe_{0.92})_2O_3$ film. Also shown in Fig. 3(a) is a Fe 2p reference spectrum for an undoped α-Fe_2O_3(0001) film. Spectra for the slow-grown films are identical to those for fast-grown films. Although these spectra indicate only Fe^{3+} and Ti^{4+} with no detectable Fe^{2+} or Ti^{3+}, it has been shown that the observation of states at the top of the valence band in iron oxides provides a more sensitive measure of the valence state(s) of iron.[26] Previous investigation

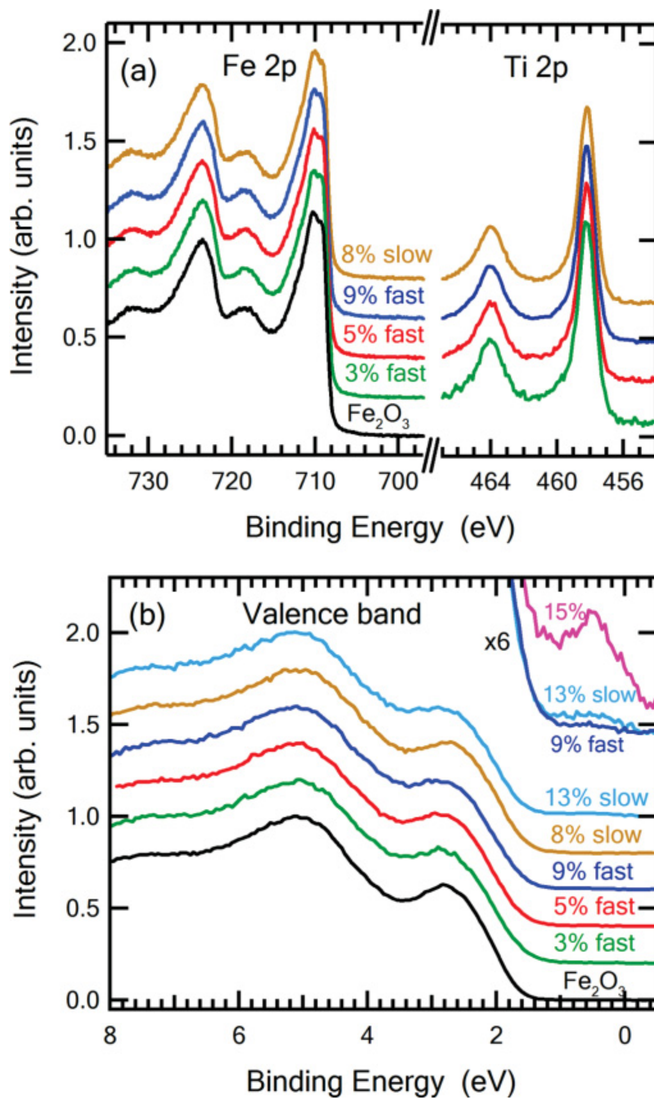

FIG. 3. (Color online) (a) Fe 2p, Ti 2p, and (b) valence band x-ray photoelectron spectra for fast-grown $(Ti_xFe_{1-x})_2O_3$ films ($x = 0.03$, 0.05, 0.09) and a representative slow-grown $(Ti_{0.08}Fe_{0.92})_2O_3$ film, along with spectra for a pure Fe_2O_3 film. The valence band spectra in (b) include $x = 0.13$, as well as a $(Ti_{0.15}Fe_{0.85})_2O_3$ film taken from Ref. 6.

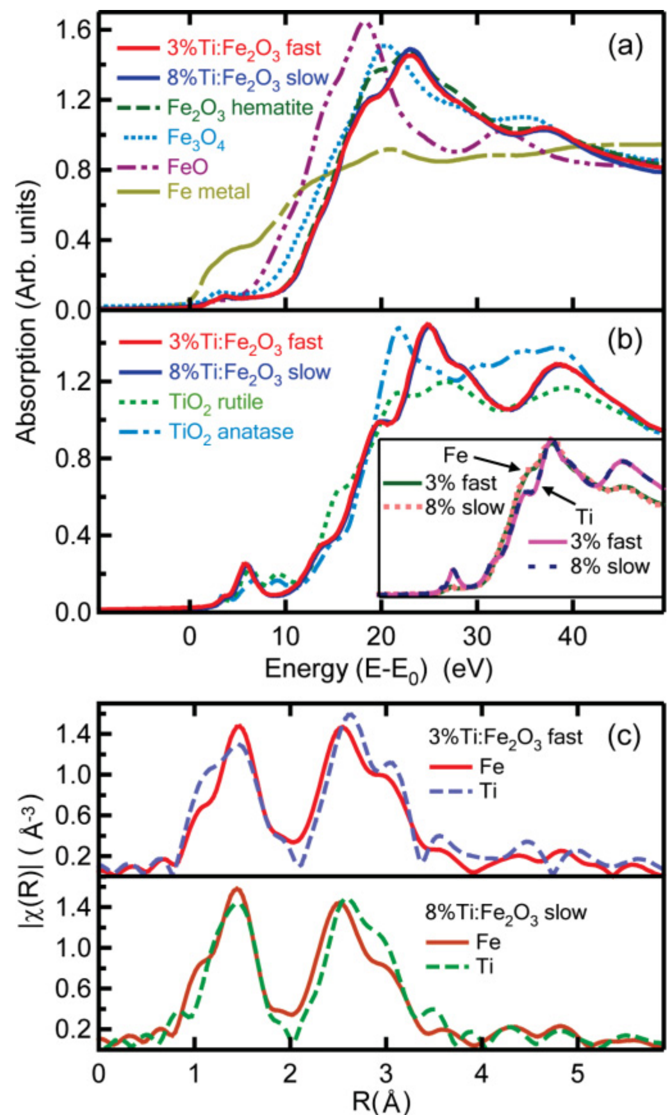

FIG. 4. (Color online) (a) Fe K-edge and (b) Ti K-edge XANES for slow-grown $(Ti_{0.08}Fe_{0.92})_2O_3$ and fast-grown $(Ti_{0.03}Fe_{0.97})_2O_3$ films, along with reference spectra for standard compounds. Inset in (b): overlapped Ti K-shell and Fe K-shell leading edges. (c) Fe and Ti K-edge EXAFS radial distribution functions for the same two films.

of $Ti:Fe_2O_3$ thin films indicated a weak Fe^{2+} feature at the top of the valence band for $x = \sim 0.15$.[6] In the valence band spectra plotted in Fig. 3(b), no such feature is seen up to $x = 0.09$. However, a weak feature is observed for slow-grown $(Ti_{0.13}Fe_{0.87})_2O_3$, indicating the presence of a low concentration of Fe^{2+} in this film.

Similar conclusions about the cation charge states are drawn from XANES. We show in Figs. 4(a) and (b) Fe and Ti K-edge spectra for representative slow- and fast-grown films. Comparison of the inflection point along the Fe leading absorption edge with those from reference spectra in Fig. 4(a) shows a strong similarity to pure α-Fe_2O_3, revealing that the vast majority of Fe is present as Fe^{3+}. Comparison of Ti K-shell XANES in Fig. 4(b) with those for TiO_2 anatase and rutile are consistent with Ti being present as Ti^{4+}. Interestingly, the overall line shapes of the Ti K-shell XANES from the $(Ti_xFe_{1-x})_2O_3$ films more closely resemble those of the corresponding Fe K-shell XANES than those associated with the Ti K-edge for TiO_2 polymorphs, as seen in the inset of Fig. 4(b), suggesting that Ti substitutes for Fe in the hematite lattice rather than forming a secondary phase such as anatase or rutile. Ti substitution for Fe was further confirmed by the similarity between Ti and Fe K-edge EXAFS radial distribution functions, shown in Fig. 4(c), which reveals that the nearest- and next-nearest-neighbor bond lengths of Ti and Fe are similar. Because of the similar values for the Ti^{4+} and Fe^{3+} ionic radii, we do not expect large changes in the local environment caused by Ti doping. Comparison of XANES and EXAFS for fast- and slow-grown films shows that they are essentially the same, indicating no substantial difference in local structure or charge states for the two growth rates, consistent with RHEED, XRD, and XPS results.

D. Electrical transport

Bench top colinear four-point probe measurements with spring-loaded contacts show that all Ti-doped Fe_2O_3 slow-grown films are highly resistive ($\rho \geqslant \sim 10^3\ \Omega \cdot$ cm), whereas all fast-grown Ti-doped films are modestly conductive ($\rho \sim 1\ \Omega \cdot$ cm) at room temperature. In contrast, pure Fe_2O_3 films grown under identical conditions at both growth rates were highly resistive. Further transport measurements were done only on the fast-grown Ti-doped films.

The resistivity as a function of temperature is shown in Fig. 5 for the fast-grown films. The increases in resistivity with decreasing temperature indicate that all films are semiconducting. The room-temperature resistivities of all fast-grown $(Ti_xFe_{1-x})_2O_3$ films decrease from 1.5 to 0.3 $\Omega \cdot$ cm with increasing x. The resistivities increase by approximately five orders of magnitude as the temperature is reduced to 50 K for all Ti concentrations.

The Hall data are summarized in Fig. 6. The dependence of V_H/I on magnetic field (B) is seen in the inset of Fig. 6(a), where the Hall coefficient is determined. The negative slope indicates n-type conduction. The Hall coefficient (R_H) is related to the concentration and mobility of both types of carriers,[28]

$$R_H = \frac{-n\mu_e^2 + p\mu_h^2}{e(n\mu_e + p\mu_h)^2}. \tag{1}$$

Here e is the absolute value of the electron charge, n and μ_e are the electron concentration and mobility, respectively, and p and μ_h are the hole concentration and mobility, respectively. Predominantly n-type conduction agrees with previous studies, which reveal that electrons are the majority carrier in Ti-doped hematite.[15,29] In addition, hole mobility in hematite has been predicted to be lower than electron mobility.[30,31] Thus, we expect the Hall coefficient for Ti-doped hematite to be dominated by the electron terms, simplifying Eq. (1) to that of an intrinsic n-type semiconductor,

$$R_H = -\frac{1}{ne}. \tag{2}$$

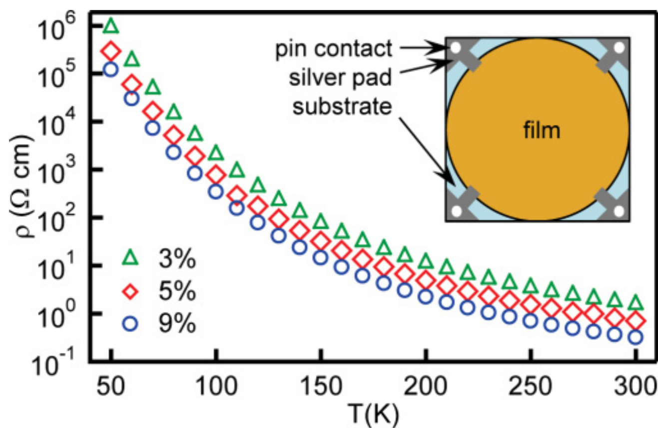

FIG. 5. (Color online) Resistivity vs temperature for fast-grown $(Ti_xFe_{1-x})_2O_3$ with $x = 0.03$, 0.06, and 0.09. A schematic diagram of the contacts is shown in the inset.

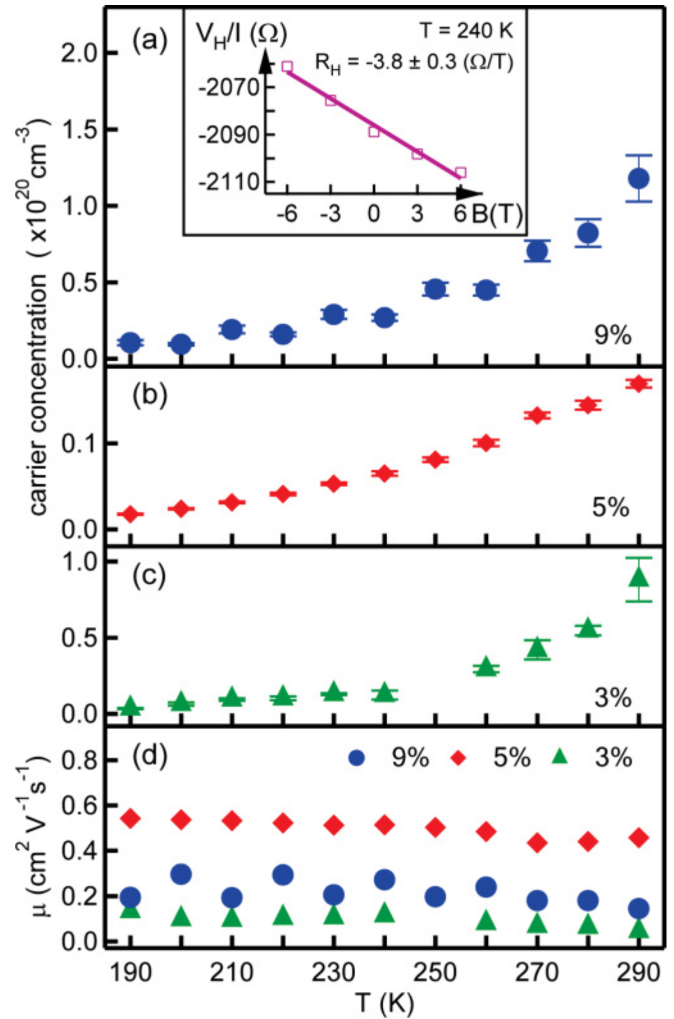

FIG. 6. (Color online) (a)–(c) Carrier concentration vs temperature from 190 K to 290 K for fast-grown $(Ti_xFe_{1-x})_2O_3$ with $x = 0.03$, 0.06, and 0.09. Inset in (a): V_H/I vs magnetic field for $x = 0.09$ film. (d) Mobility vs temperature determined from carrier concentration and resistivity data.

The carrier concentrations derived from the Hall coefficient using Eq. (2) are shown in Figs. 6(a)–(c). The room-temperature carrier concentrations range from 2×10^{19} to 1×10^{20} cm^{-3} and decrease with decreasing temperature. Hall mobilities were calculated using the equation

$$\mu = \frac{1}{e\rho n}, \tag{3}$$

where e is the charge of an electron, ρ is resistivity, and n is carrier concentration. The results are shown in Fig. 6(d). The mobilities for the three fast-grown films range from $\sim$0.1 to $\sim$0.6 cm^2/V $\cdot$ s, consistent with previous experimental studies,[9,15,31] and do not vary significantly with temperature. Surprisingly, the carrier concentrations and mobilities do not scale with Ti concentration as one might expect based on each Ti being an uncompensated donor.

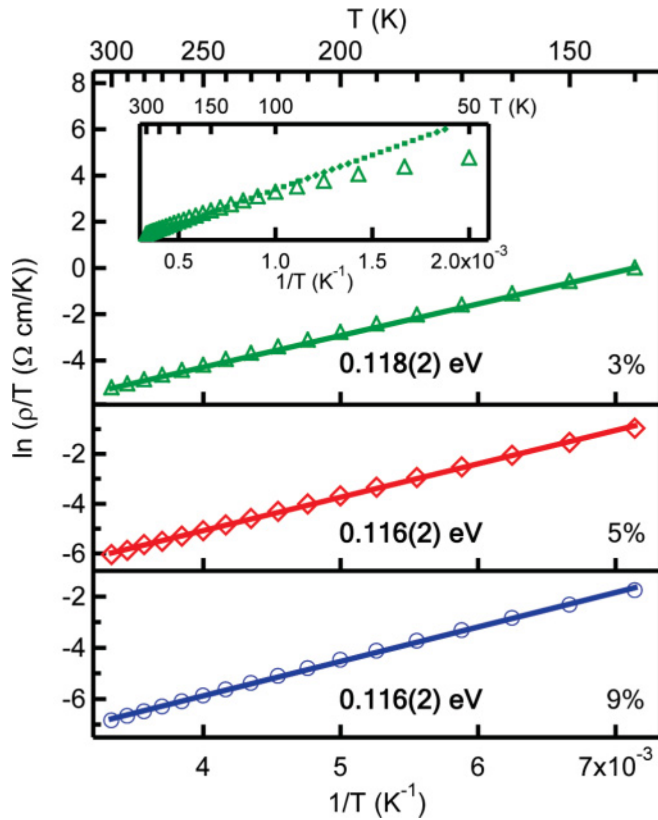

FIG. 7. (Color online) Fits of resistivity vs temperature data to the small polaron hopping model from 300 K to 140 K for fast-grown $(Ti_xFe_{1-x})_2O_3$ with $x = 0.03$, 0.06, and 0.09. Inset: deviation of the experimental data from the small polaron hopping model at temperatures below 140 K is shown for $x = 0.03$.

E. Comparison with transport models

Different mechanisms of conduction can be explored by comparing the transport data to model predictions. In transition metal oxides where electron-phonon coupling is usually significant due to high bond polarity, an itinerant electron tends to polarize its immediate surroundings to lower its energy.[13] The electron and its polarized local structure constitute a quasiparticle called a polaron. The polaron effective mass is considerably higher than that of a free electron, resulting in lower electron mobility in such lattices. In most previous transport studies for hematite, the mechanism of conductivity was taken to be the small polaron hopping model at temperatures above half of the Debye temperature,[13,32] which has been estimated to be $\Theta_D/2 \sim 200$ K.[33,34] In this model, small polarons conduct through thermally activated hopping from one site to another. The relationship between resistivity and temperature is given by[35]

$$\rho(T) \propto T \exp\left(\frac{E_a}{k_B T}\right). \tag{4}$$

Here E_a is the activation energy for hopping and k_B is the Boltzmann constant. Figure 7 shows small polaron model fits to the resistivity-temperature data from room temperature to 140 K for all three Ti concentrations. Activation energies determined from the slopes of the fit lines are 0.118 ± 0.002 eV, 0.116 ± 0.002 eV, and 0.116 ± 0.002 eV for $x = 0.03$, 0.05, and 0.09, respectively. These activation energies agree remarkably well with the 0.11 eV calculated by *ab initio* theory,[13] as well as 0.1 eV estimated for hematite basal-plane conduction given by Goodenough *et al.*[11] and 0.08 eV from Gharibi *et al.*[12] Thus, conductivity from 300 to 140 K for all Ti concentrations is consistent with small polaron hopping and an activation barrier of ~0.1 eV. For temperatures well below $\Theta_D/2$, the small polaron hopping probability rapidly decreases and the polaron hopping model no longer applies,[36] as seen in the inset for Fig. 7.

TABLE I. Electrical transport summary for fast-grown $(Ti_xFe_{1-x})_2O_3$ epitaxial films.

Film	ρ ($\Omega\cdot$cm) at 290 K	n (cm^{-3}) at 290 K	μ (V/cm$^2\cdot$s) at 290 K	E_a (eV) from ρ(T)
$(Ti_{0.03}Fe_{0.97})_2O_3$	1.74	8.8E + 19	0.04	0.118(2)
$(Ti_{0.05}Fe_{0.95})_2O_3$	0.80	1.7E + 19	0.46	0.116(2)
$(Ti_{0.09}Fe_{0.91})_2O_3$	0.37	1.2E + 20	0.14	0.116(2)

The applicability of the small polaron hopping model in the high-temperature range can also be examined using mobility data. It has been predicted that in materials where small polarons are formed, the intrinsic mobility would be of the order of 0.1 ~ 1 cm^2/V · s,[37] which is lower than that of more typical semiconductors (for example, at 300 K μ_e ~7 × 10^3 cm^2/V · s for GaAs[38] and ~1 × 10^1 cm^2/V · s for La:$SrTiO_3$[39]). The mobilities for the present samples range from ~0.1 to ~0.6 cm^2/V · s, comparable to that expected for small polarons. Moreover, these values are in good agreement with previous theoretical studies on hematite transport using a small polaron hopping model.[13] Table I shows a summary of transport results at 290 K along with activation energies from the fits of the resistivity data to the small polaron hopping model.

An alternative conduction model that is often hypothesized for doped systems is variable-range hopping (VRH), in which a carrier hops between localized states created by randomly distributed dopants.[40,41] There are several different VRH mechanisms, including Mott three-dimensional (3D) VRH,[40] Mott two-dimensional (2D) VRH,[40] and Efros-Shklovskii VRH.[42] Our data fit best with Mott 2D VRH, for which conductivity follows the relation

$$\rho(T) \propto \exp[(T_0/T)^{1/3}]. \tag{5}$$

Here $T_0 = \lambda\alpha^3/k_B\rho_0$, where λ is a dimensionless constant, α is the coefficient of exponential decay of the localized states, and ρ_0 is the density of states at the Fermi level.[41] VRH is intrinsically a low-temperature process, and the model neglects other transport mechanisms that would operate at higher temperatures, such as tunneling.[40,41] The resistivity data can be fit well to the Mott 2D VRH model in the low-temperature range (180–60 K) for all Ti concentrations. These fits are shown in Fig. 8(a), and the quality of the fits lead us to conclude that the conduction mechanism at these relatively low temperatures is indeed VRH. Data taken at 50 K are not useful for the purpose of this fit because the films were so resistive that equilibration times were impractically long.

The fact that the data fit the Mott 2D model better than the Mott 3D model is not unexpected due to the magnetic structure

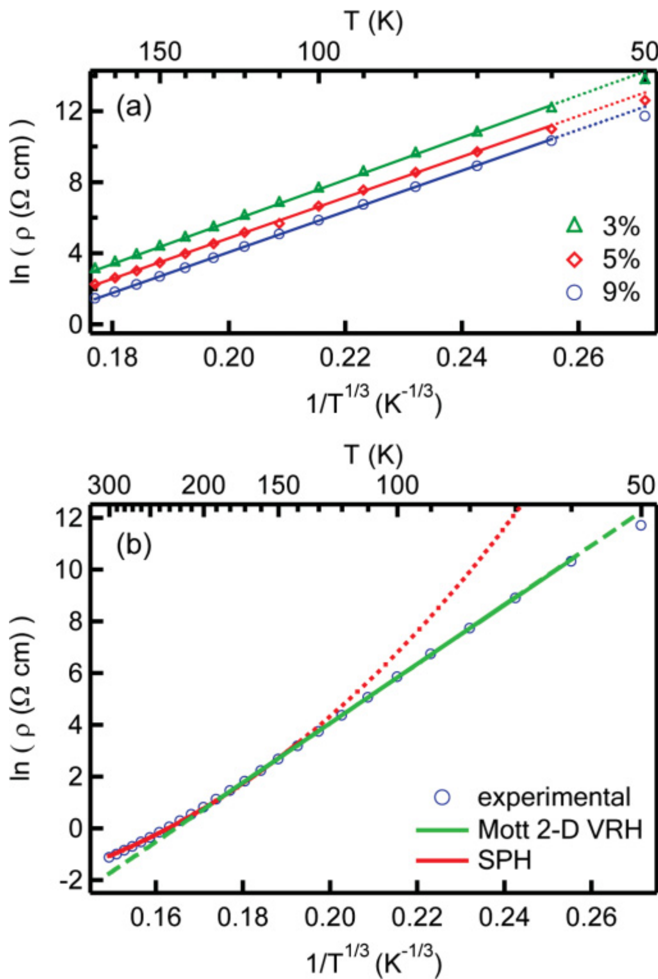

FIG. 8. (Color online) (a) Fits of the data to the Mott 2D VRH model from 180 K to 60 K for fast-grown $(Ti_xFe_{1-x})_2O_3$ with $x = 0.03$, 0.06, and 0.09. (b) Fits of the resistivity data to the small polaron hopping and VRH models for the $(Ti_{0.09}Fe_{0.91})_2O_3$ film, revealing a transition from one mechanism to the other, which occurs between 180 and140 K.

of hematite and Hund's rules, which place spin restrictions on electron transport between adjacent Fe layers separated by an O layer along the c axis. In hematite, structural Fe^{3+} cations (d^5) are in a high-spin state with all spins aligned. Moreover, all cations within a given Fe layer in the ab plane have the same spin orientation, and those in adjacent Fe layers separated by an O plane along the c direction have the opposite spin. An electron can thus migrate from Fe to Fe along the ab plane without undergoing spin flip, whereas one being transported from one Fe layer to the next along the c direction must. In previous theoretical and experimental studies, the spin-flip energy was found to be large and the mobility along the c axis was approximately three orders of magnitude lower than that within the ab plane.[14,30,43] Therefore, conductivity in hematite appears to be dominated by transport within the ab plane, consistent with the Mott 2D model rather than the 3D model.

Finally, we show in Fig. 8(b) the changeover in conduction mechanism across the two different temperature ranges for the $(Ti_{0.09}Fe_{0.91})_2O_3$ film. From the previous discussion, we conclude that the conduction mechanism in the high-temperature regime is small polaron hopping, which transitions to Mott 2D VRH in the low-temperature regime. The transition temperature is between 180 and 140 K, comparable with the previous theoretical estimation of $\Theta_D/2$ for hematite.[33,34] Such a transition from high-temperature small polaron hopping to low-temperature VRH has also been suggested to occur in other oxides such as Fe_3O_4,[44] Ni-doped $LaFeO_3$,[45] and Cr-doped rare-earth manganites.[46]

F. The effect of growth rate on conductivity

The stark difference in conductivity between films grown at the two rates was unexpected. The structural and compositional properties of the two film sets are nominally the same. Yet, the fast-grown films are semiconducting whereas the slow-grown films are highly resistive at room temperature. We conjecture that the formation of compensating cation vacancies may play a role, as has been suggested for Nb-doped TiO_2 rutile. Morris *et al.*[47] found that Nb-doped TiO_2 prepared by the solid-state reaction of NbO_2 and TiO_2 powders at elevated temperature in vacuum exhibited a Nb-derived state in the upper portion of the TiO_2 bandgap, as well as dark coloration characteristic of an n-type semiconductor. The same was found for diffusionally doped Nb:TiO_2(110) single crystals. In contrast, $Nb_xTi_{1-x}O_2/TiO_2(110)$ grown by OPA-MBE exhibited no such gaps states and was transparent as well as insulating.[48] A key difference between these two synthesis approaches was the oxygen fugacity at the growth front, which was suggested to significantly increase the equilibrium concentration of cation vacancies in OPA-MBE grown materials but not in materials prepared by solid-state reaction under vacuum.[47] In the present work, both growth rates employed the same oxygen pressure and plasma power settings. However, the relative oxygen overpressure, and thus the oxygen fugacity at the growth front, are higher when the metal flux is lower (i.e., the slower growth rate). Under O-rich conditions, as found in OPA-MBE, the relevant charged species that could in principle form during the growth of $(Ti_xFe_{1-x})_2O_3$ are ionized substitutional Ti^{4+} dopants ($Ti^{\cdot}_{Fe}$), interstitial Ti^{3+} ions ($Ti^{\cdot\cdot\cdot}_i$), structural Fe^{2+} ions (Fe'_{Fe}), interstitial Fe^{3+} ions ($Fe^{\cdot\cdot\cdot}_i$), and Fe^{3+} vacancies (V'''_{Fe}). Using Kröger-Vink notation, charge balance requires that

$$[Ti^{\cdot}_{Fe}] + 3[Fe^{\cdot\cdot\cdot}_i] + 3[Ti^{\cdot\cdot\cdot}_i] + p = n + [Fe'_{Fe}] + 3[V'''_{Fe}]. \quad (6)$$

Here p and n are hole and electron free carrier concentrations, respectively. Structural Fe^{2+} was shown by XPS and XANES to be negligible for all but the highest Ti concentration. Although slow-grown $(Ti_{0.13}Fe_{0.87})_2O_3$ exhibited a small concentration of Fe^{2+}, the film was highly resistive, indicating that structural Fe^{2+} does not contribute to hopping conduction. The extent of donor interstitial Fe^{3+} formation is negligible, since pure Fe_2O_3 films grown at both fast and slow growth rates are highly resistive. Interstitial Ti was determined to be negligible from characterization results presented previously. However, it has been shown that cation vacancies readily form during the oxidation of magnetite (Fe_3O_4) to hematite via

the intermediate maghemite (γ-Fe_2O_3), revealing that cation vacancies are stable in the various iron oxide lattices.[49] Thus, the net carrier concentration is given by

$$n - p = [Ti^{\cdot}_{Fe}] - 3[V'''_{Fe}]. \quad (7)$$

It is clear from Eq. (7) that the net electron carrier concentration can range from the Ti dopant concentration to zero, depending on the extent to which cation vacancies form. First principles calculations of point defect formation energies in n-type ZnO reveal that the formation energy of Zn vacancies is the lowest among native point defects under oxygen-rich conditions[50] and continues to drop with decreasing Zn/O ratio.[51] If a similar trend is followed in α-Fe_2O_3, we expect the Fe vacancy concentration to increase in films grown with lower Fe flux. Additionally, the extent of cation vacancy creation was previously concluded to be very sensitive to growth conditions such as temperature.[47] The same sensitivity in the present case could explain why the carrier concentration does not scale with Ti concentration (see Fig. 6).

IV. CONCLUSIONS

We have successfully grown $(Ti_xFe_{1-x})_2O_3$ epitaxial films ($x \leqslant 0.13$) at two different growth rates by OPA-MBE. Characterization shows good single crystallinity, charge states of Fe^{3+} and Ti^{4+} for $x \leqslant 0.09$, Ti substitution on Fe sites, and no substantial structural difference between films at the two growth rates. However, all fast-grown films are semiconducting whereas all slow-grown films are highly resistive. This difference is attributed to donor electron compensation by cation vacancy formation in slow-grown films, for which the oxygen-to-metal flux ratio (oxygen fugacity) is higher during growth. Resistivity and Hall measurements on fast-grown films reveal carrier concentrations of the order of $\sim 10^{19}$–10^{20} cm^{-3} at room temperature and mobilities of ~ 0.1–0.6 V/cm$^2 \cdot$ s. The low mobilities and temperature dependence of the resistivity reveal a small polaron hopping conduction mechanism at higher temperature, transitioning to VRH at lower temperature.

ACKNOWLEDGMENTS

B.Z. acknowledges fruitful discussions with Kevin Rosso, Cigdem Capan, Shawn Chatman, and Liang Qiao. B.Z. (4 months), T.C.K., T.C.D., J.M., M.E.B, V.S, and S.A.C. were supported by the Office of Science, Division of Materials Sciences and Engineering, US Department of Energy (US DOE). This work was performed in the Environmental Molecular Sciences Laboratory, a national scientific user facility sponsored by the Office of Biological and Environmental Research of the US DOE and located at Pacific Northwest National Laboratory. B.Z. (18 months) was supported by the US National Science Foundation (CHE 0628252-CRC). Use of the Advanced Photon Source, an Office of Science User Facility operated for the US DOE Office of Science by Argonne National Laboratory, was supported by the US DOE under Contract No. DE-AC02-06CH11357.

*tiffany.kaspar@pnnl.gov

[1] G. E. Brown, V. E. Henrich, W. H. Casey, D. L. Clark, C. Eggleston, A. Felmy, D. W. Goodman, M. Gratzel, G. Maciel, M. I. McCarthy, K. H. Nealson, D. A. Sverjensky, M. F. Toney, and J. M. Zachara, Chem. Rev. **99**, 77 (1999).
[2] Y.-S. Hu, A. Kleiman-Shwarsctein, A. J. Forman, D. Hazen, J.-N. Park, and E. W. McFarland, Chem. Mater. **20**, 3803 (2008).
[3] S. K. Mohapatra, S. E. John, S. Banerjee, and M. Misra, Chem. Mater. **21**, 3048 (2009).
[4] A. Patzelt, H. M. Li, J. D. Wang, and E. Appel, Tectonophysics **259**, 259 (1996).
[5] P. W. Schmidt, G. E. Williams, and B. J. J. Embleton, Earth. Planet. Sci. Lett. **105**, 355 (1991).
[6] T. Droubay, K. M. Rosso, S. M. Heald, D. E. McCready, C. M. Wang, and S. A. Chambers, Phys. Rev. B **75**, 104412 (2007).
[7] B. Gilbert, C. Frandsen, E. R. Maxey, and D. M. Sherman, Phys. Rev. B **79**, 035108 (2009).
[8] F. J. Morin, Phys. Rev. **93**, 1195 (1954).
[9] H. J. Van Daal and A. J. Bosman, Phys. Rev. **158**, 736 (1967).
[10] A. J. Bosman and H. J. van Daal, Adv. Phys. **19**, 1 (1970).
[11] J. B. Goodenough, Prog. Solid State Chem. **5**, 145 (1971).
[12] E. Gharibi, A. Hbika, B. Dupre, and C. Gleitzer, Eur. J. Solid State Inorg. Chem. **27**, 647 (1990).
[13] K. M. Rosso, D. M. A. Smith, and M. Dupuis, J. Chem. Phys. **118**, 6455 (2003).
[14] T. Nakau, J. Phys. Soc. Jpn. **15**, 727 (1960).
[15] F. J. Morin, Phys. Rev. **83**, 1005 (1951).
[16] G. A. Acket and J. Volger, Physica **32**, 1543 (1966).
[17] S. A. Chambers, Y. Liang, and Y. Gao, Phys. Rev. B **61**, 13223 (2000).
[18] H. Muta, K. Kurosaki, M. Uno, and S. Yamanaka, J. Alloys Compd. **335**, 200 (2002).
[19] J. A. Glasscock, P. R. F. Barnes, I. C. Plumb, and N. Savvides, J. Phys. Chem. C **111**, 16477 (2007).
[20] N. Uekawa, M. Watanabe, K. Kaneko, and F. Mizukami, J. Chem. Soc., Faraday Trans. **91**, 2161 (1995).
[21] J. S. McCloy, J. V. Ryan, T. Droubay, T. C. Kaspar, S. Chambers, and D. C. Look, Rev. Sci. Instrum. **81**, 063902 (2010).
[22] D. C. Look, *Electrical Characterization of GaAs Materials and Devices*, (John Wiley & Sons, Chichester, 1989), Chap. 1.
[23] J. A. Maxwell, J. L. Campbell, and W. J. Teesdale, Nucl. Instrum. Methods Phys. Res., Sect. B **43**, 218 (1989).
[24] T. C. Kaspar, T. Droubay, V. Shutthanandan, S. M. Heald, C. M. Wang, D. E. McCready, S. Thevuthasan, J. D. Bryan, D. R. Gamelin, A. J. Kellock, M. F. Toney, X. Hong, C. H. Ahn, and S. A. Chambers, Phys. Rev. B **73**, 155327 (2006).
[25] E. N. Maslen, V. A. Streltsov, N. R. Streltsova, and N. Ishizawa, Acta Crystallogr. Sect. B-Struct. Commun. **50**, 435 (1994).
[26] R. D. Shannon, Acta Cryst. A **32**, 751 (1976).
[27] B. A. Wechsler and C. T. Prewitt, Am. Mineral. **69**, 176 (1984).
[28] D. K. Schroder, *Semiconductor Material and Device Characterization* (John Wiley & Sons, New York, 2006), p. 94.

[29] P. Liao, M. C. Toroker, and E. A. Carter, Nano Lett. **11**, 1775 (2011).

[30] N. Iordanova, M. Dupuis, and K. M. Rosso, J. Chem. Phys. **122**, 144305 (2005).

[31] R. F. G. Gardner, F. Sweett, and D. W. Tanner, J. Phys. Chem. Solids **24**, 1175 (1963).

[32] P. L. Liao, M. C. Toroker, and E. A. Carter, Nano Lett. **11**, 1775 (2011).

[33] S. Kerisit and K. M. Rosso, Geochim. Cosmochim. Acta **70**, 1888 (2006).

[34] S. Kerisit and K. M. Rosso, J. Chem. Phys. **127**, 124706 (2007).

[35] I. G. Austin and N. F. Mott, Adv. Phys. **18**, 41 (1969).

[36] T. Holstein, Ann. Phys. **8**, 343 (1959).

[37] D. Emin, C. H. Seager, and R. K. Quinn, Phys. Rev. Lett. **28**, 813 (1972).

[38] S. M. Sze and J. C. Irvin, Solid-State Electron. **11**, 599 (1968).

[39] J. Son, P. Moetakef, B. Jalan, O. Bierwagen, N. J. Wright, R. Engel-Herbert, and S. Stemmer, Nat. Mater. **9**, 482 (2010).

[40] N. F. Mott, Philos. Mag. **19**, 835 (1969).

[41] V. Ambegaokar, B. I. Halperin, and J. S. Langer, Phys. Rev. B **4**, 2612 (1971).

[42] A. L. Efros and B. I. Shklovskii, J. Phys. C: Solid State Phys. **8**, L49 (1975).

[43] D. Benjelloun, J. P. Bonnet, J. P. Doumerc, J. C. Launay, M. Onillon, and P. Hagenmuller, Mater. Chem. Phys. **10**, 503 (1984).

[44] F. Walz, J. Phys.: Condens. Matter **14**, R285 (2002).

[45] M. W. Khan, S. Husain, M. A. M. Khan, M. Gupta, R. Kumar, and J. P. Srivastava, Philos. Mag. **90**, 3069 (2010).

[46] A. Banerjee, S. Pal, and B. K. Chaudhuri, J. Chem. Phys. **115**, 1550 (2001).

[47] D. Morris, Y. Dou, J. Rebane, C. E. J. Mitchell, R. G. Egdell, D. S. L. Law, A. Vittadini, and M. Casarin, Phys. Rev. B **61**, 13445 (2000).

[48] S. A. Chambers, Y. Gao, Y. J. Kim, M. A. Henderson, S. Thevuthasan, S. Wen, and K. L. Merkle, Surf. Sci. **365**, 625 (1996).

[49] S. Nasrazadani and A. Raman, Corros. Sci. **34**, 1355 (1993).

[50] A. Janotti and C. G. Van de Walle, Phys. Rev. B **76**, 165202 (2007).

[51] A. F. Kohan, G. Ceder, D. Morgan, and C. G. Van deWalle, Phys. Rev. B **61**, 15019 (2000).